SrSnO$_3$-Assembled MWCNT Heterojunctions for Superior Hydrogen Production under Visible Light

Mohammad W. Kadi and Reda M. Mohamed*

Read Online

ACCESS | Metrics & More | Article Recommendations | Supporting Information

ABSTRACT: A one-step sol−gel method for SrSnO$_3$ nanoparticle synthesis and the incorporation of multi-walled carbon nanotubes (MWCNTs) to produce a SrSnO$_3$@MWCNT photocatalyst is presented. The incorporation of MWCNTs results in enhancement of structural, optical, and optoelectrical properties of SrSnO$_3$. The optimized 3.0% addition of MWCNTs results in light absorption enhancement and a reduction of the band gap from 3.68 to 2.85 eV. Upon application of the photocatalyst in the photocatalytic hydrogen production reaction, SrSnO$_3$@MWCNT-3.0% yields 4200 μmol g^{-1} of H$_2$ in just 9 h with the use of 1.6 g L^{-1} of the photocatalyst. SrSnO$_3$@MWCNT exhibits remarkable chemical and photocatalytic stability upon regeneration. Enhanced photocatalytic ability is attributed to improved surface properties and charge-carrier recombination suppression induced by the MWCNT addition. This study highlights the remarkable improvements in chemical and physical properties of semiconductors with MWCNT incorporation.
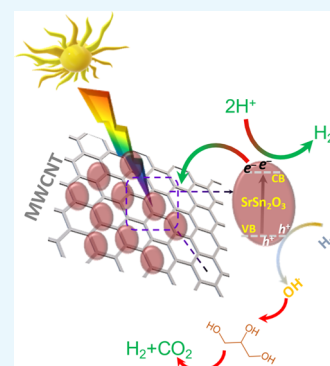
1. INTRODUCTION

The ever-increasing energy demand and environmental concerns led researchers to increase their efforts for a search of clean and sustainable energy sources.[1−5] Harvesting the energy emitted by the Sun is a major point of interest. One important aspect in utilizing Sun's energy is its storage as chemical energy in the form of hydrogen. Photocatalytic hydrogen production has received considerable attention and is still an active area of research.[6] Photocatalytic hydrogen production can be achieved by constructing a material that produces electron−hole pairs upon irradiation. By controlling the flow of the charge carriers, the electrochemical reaction between photoelectrons and H$^+$ species in the aqueous media will result in H$_2$ generation.[7] Honda and Fujishima used TiO$_2$ and UV light to split water to produce hydrogen for the first time.[8] Inspired by this breakthrough, many researchers explored all aspects that can improve hydrogen production via this route. A major aspect being the use of visible light to induce photocatalysis as visible light constitutes more than 40% of the emitted energy of the Sun.[4,9−14] In constructing a photocatalyst, one must consider many factors that are detrimental to the efficiency of materials. These factors include the crystal structure, the energy of the band gap, and the surface area of the materials. Many strategies have been applied to achieve desirable band energies, morphology, and high surface areas. Examples of applied strategies include heteroatom doping, control of the nanometer size of the materials, and the control of pore volumes and numbers.[15,16]

In recent years, perovskite semiconductors have been shown to possess properties that can be utilized in wide range applications in renewable energy and environmental remediation.[17−21] Perovskites have been applied in water splitting and photocatalytic degradation of toxic compounds.[22−25] For example, alkaline-earth stannates are ferromagnetic perovskites with distinctive properties as they are piezo- and pyroelectric materials. These properties allow their utilization in capacitors, photoluminescent devices, sensors, many electronic devices, and as photocatalysts.[26−30] SrSnO$_3$ has a three dimensional crystal structure in which SnO$_6$ octahedral and SrSnO$_3$ octahedral distortions promote electron/hole mobility and separation, yielding effective photocatalysis as has been shown in several studies of organic pollutant degradations.[31−35] SrSnO$_3$ was also used in humidity sensors,[36] lithium ion batteries,[37] thermal capacitors,[38] and in electronic devices.[39]

To improve the photocatalytic activity of a material, consistent separation of electron hole pairs must be achieved.[40−46] This can be done by incorporating noble metals or nanostructured carbon materials as modifiers or cocatalysts.[47−51] Multiwalled carbon nanotubes (MWCNTs) have high electron storage capacity, have a very large specific surface area, superior metallic conductivity, and are mechanically and chemically very stable.[52−54] Their use, for example, with anatase TiO$_2$ resulted in enhanced photocatalytic performance through the creation of a heterojunction on TiO$_2$ surfaces.[55,56] They can also act as electron sinks

separating them from holes and allowing electrons to create reactive radicals such as superoxide ($O_2^{\bullet-}$) and hydroxyl radicals that facilitate photocatalysis.[57,58] In this paper, we report the synthesis of mesoporous $SrSnO_3$ using a simple sol–gel method in the presence of nonionic surfactant Pluronic F-127. The effect of addition of different weight percentages of MWCNTs on the physical and photocatalytic performances of mesoporous $SrSnO_3$ for production of hydrogen under visible light is studied.

2. EXPERIMENTAL SECTION

2.1. Materials. Polyethylene oxide–propylene oxide tri-block copolymer (PEO/PPO/PEO), average M_n ~12,600, known as the Pluronic F-127 surfactant, $Sr(NO_3)_2$, $SnCl_4 \cdot 5H_2O$, CH_3COOH, HCl, and C_2H_5OH were purchased from Sigma-Aldrich. MWCNTs (>95%) were also obtained from Sigma-Aldrich.

2.2. Synthesis of Mesoporous $SrSnO_3$. 0.3 g Pluronic F-127 was dissolved in 30 mL of C_2H_5OH, followed by the addition of 2.1 g $Sr(NO_3)_2$ and 2.6 g of $SnCl_4 \cdot 5H_2O$ gradually with continuous stirring. 0.82 mL of HCl and 2.7 mL of CH_3COOH were added to the solution with stirring for additional 1 h allowing the sol to develop. The sol was dried at 40 °C in 40–80% humidity, followed by 12 h drying at 65 °C. The product was calcined at 700 °C.

2.3. MWCNT Activation. 30–40 nm diameter MWCNTs were used in the synthesis process. MWCNTs were activated using concentrated HNO_3. In this process, 0.25 g of the nanotubes were added to 100 mL of 6 M HNO_3 in a three-neck flask and refluxed at 120 °C for 6 h. This step will eliminate amorphous carbon and other contaminants and will functionalize the outer walls of tubes with carboxylic groups, which will allow $SrSnO_3$ crystal incorporation. After refluxing, activated MWCNTs were sieved and rinsed several times with H_2O. The water was evaporated overnight at 110 °C.

2.4. Preparation of $SrSnO_3$-MWCNT Nanocomposites. A desired amount of the activated MWCNT was dispersed in a 2:1 H_2O and ethanol mixture and sonicated for 30 min, followed by $SrSnO_3$ addition. The mixture was dried at 60 °C for 12 h resulting in mesoporous $SrSnO_3$@MWCNT nano-composites with the $SrSnO_3$ nanoparticles attached at the MWCNT surface. MWCNT/$SrSnO_3$ nanocomposites with MWCNT weight percentages of 1, 2, 3 and 4 wt % were prepared by adding 0.01, 0.02, 0.03, and 0.04 g separately to 1.0 g of $SrSnO_3$ in four independent samples.

2.5. Characterizations of Photocatalysts. X-ray diffraction (XRD) and X-ray photoelectron spectroscopy (XPS) were utilized to investigate the crystal structure and elemental oxidation states of the nanocomposites For this Bruker axis D8, Cu Kα radiation, and XPS, Thermo Scientific, were utilized. A transmission electron microscope (JEOL-JEM-1230) was used to obtain transmission electron microscopy (TEM) and high-resolution TEM (HR-TEM) images of the dispersed materials on carbon-coated TEM grids. Adsorption/desorption iso-therms and consequently the specific surface area (S_{BET}) were determined utilizing a Chromatech device (Nova 2000). Light absorption capacity of the photocatalyst was estimated using a V-570 (JASCO) spectrophotometer in the range of 200–800 nm. Diffusive reflectance (DR) spectra and the Kubelka–Munk formula were used to calculate E_g of the semiconductors. The photoluminescence (PL) response of all the samples was obtained using a Shimadzu RF-5301 fluorescence spectrom-eter. The Zennium-Zahner electrochemical system was used to

measure the photocurrent response of all samples blended on conductive substrates of 0.5 cm^{-2} size.

2.6. Photocatalytic Activity. The photocatalytic efficiency of the $SrSnO_3$ and $SrSnO_3$@MWCNT nanocomposites was measured from H_2 yield from glycerol solutions upon visible light irradiation using a Pyrex photoreactor. $SrSnO_3$ and $SrSnO_3$@MWCNT nanocomposites (50 mg) were suspended separately in glycerol (10 vol % in 200 mL of water) by stirring and loaded to the photoreactor. Prior to the photocatalytic reaction, the photoreactor was bubbled with Argon flow (300 mL/min) for 10 min to purge the oxygen in the photocatalyst suspension. A 500 W Xe lamp (UV cutoff filter > 420 nm) located vertically on the top of the photoreactor was used for illuminating the solution. An Agilent GC 7890A system was utilized to quantify hydrogen evolution during the course of the photocatalytic reaction for 9 h with gas sampling at 60 min intervals.

3. RESULTS AND DISCUSSION

3.1. Photocatalyst Characterizations. The XRD pat-terns of pure $SrSnO_3$, pure MWCNT, and the $SrSnO_3$@MWCNT nanocomposite samples are shown in Figure 1. The
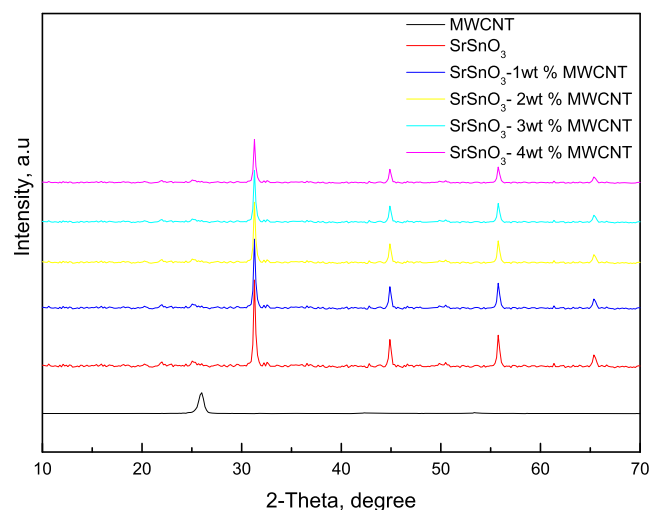

Figure 1. XRD patterns of $SrSnO_3$, MWCNTs, and $SrSnO_3$@MWCNT.

peak at 25.9° confirms the presence of (002) of MWCNTs in the pure sample (JCPDS card no. 26-1079). Both pure $SrSnO_3$ and $SrSnO_3$@MWCNT samples show diffraction peaks consistent with the crystalline planes of the pure $SrSnO_3$ (JCPDS no. 77-1798).[33,35] However, no MWCNT peaks appear in all $SrSnO_3$@MWCNT samples, most probably because of low concentrations. It is also notable that crystallite sizes were smaller in all $SrSnO_3$@MWCNT samples as the addition of the nanotubes hinders $SrSnO_3$ particle agglomer-ation.

The $SrSnO_3$@MWCNT-3% sample was subjected to high-resolution XPS, and the spectra are shown in Figure 2. The XPS signals were calibrated with the standard C 1s peak at 284.8 eV. Two overlapping peaks for the two 3d orbitals of the Sr atom are shown in Figure 2A with Sr3d5/2 at 132.7 eV and Sr3d3/2 at 134.5 eV, and the separation between the two is ~1.8 eV hence the overlap at this resolution.[34] On the other hand, for the Sn atom the same two energy levels are well separated, 3d5/2 at 486.3 eV and 3d3/2 at 494.8 eV as shown

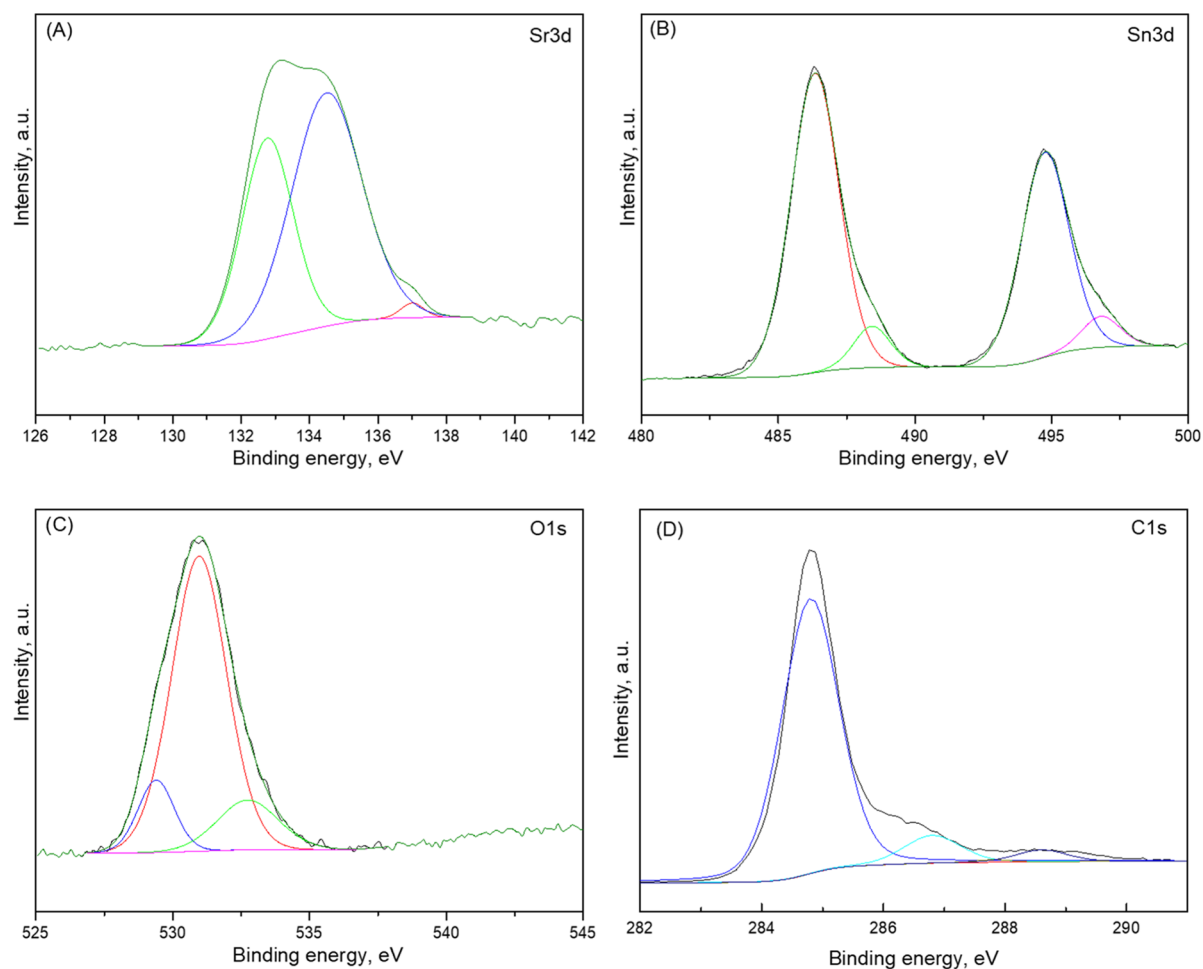**Figure 2.** High-resolution XPS spectra of Sr 3d (A), Sn 3d (B), O 1s (C), and C 1s (D) of SrSnO$_3$@MWCNT-3 wt %.
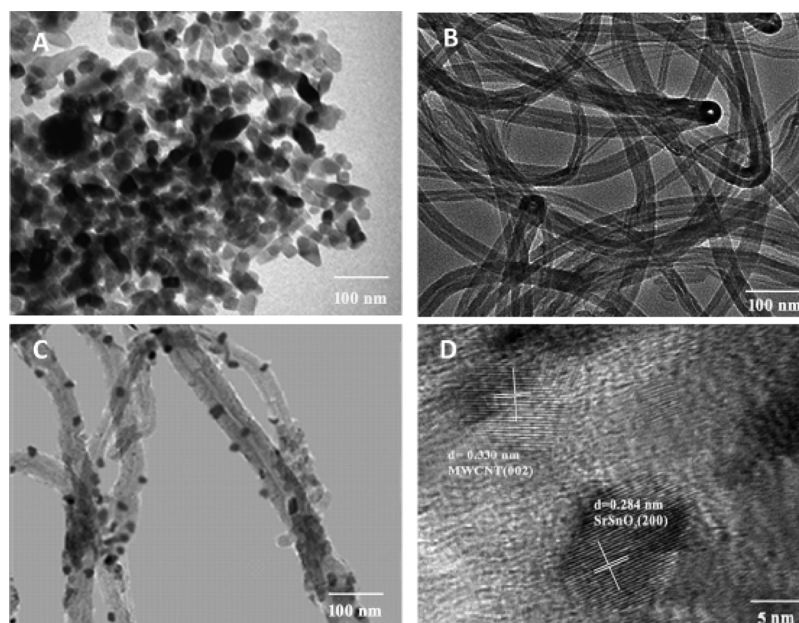

Figure 3. TEM images of (A) SrSnO$_3$, (B) MWCNTs, and (C) SrSnO$_3$@MWCNT, and (D) HRTEM image of SrSnO$_3$@MWCNT-3 wt %.

in Figure 2B. The 1s orbital of oxygen shows at slightly different positions depending on the chemical state of the atom in the crystal structure (Figure 2C). The 529.4 eV peak is attributed to the O^{2-} ions within the lattice structure, the 530.9 eV peak is attributed to the O^{2-} ions in the O-deprived areas in the structure, and the 532.4 eV peak can be attributed to the loosely bound O atoms of O$_2$ and H$_2$O molecules adsorbed on the surface of the lattice structure.[33] Orbitals of the three

atoms confirm the crystal structure of $SrSnO_3$. As for MWCNTs, the energy of the 1s of carbon atoms at 284.8 eV indicates the presence of the C−C bond in the nanotubes, while C−O band shows at 286.8 eV.

The TEM images of pure $SrSnO_3$, pure MWCNT, and $SrSnO_3$@MWCNT nanocomposite samples are presented in Figure 3A−C, respectively. $SrSnO_3$ appears as nanoparticles with an average size of 20 nm. As shown in Figure 3B, the nanotubes are pure with no metal or carbon impurities. The nanocomposites in Figure 3C show scattered $SrSnO_3$ particles on the nanotube surface. In HRTEM images, for $SrSnO_3$@MWCNT-3 wt %, the 0.284 nm d-spacing shows the incorporation of $SrSnO_3$ into the nanocomposite, while the (002) at 0.330 nm confirms the incorporation of MWCNTs into the nanocomposite (Figure 3D).

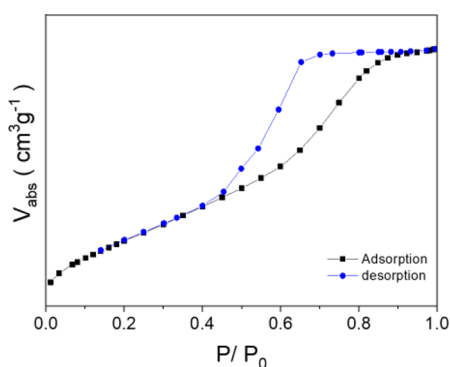Type IV isotherm as is evident from Figure 4 of the adsorption−desorption data for the $SrSnO_3$@MWCNT-3 wt

Figure 4. Adsorption−desorption isotherm of $SrSnO_3$@MWCNT-3 wt %.

% sample reveals the mesoporous nature of the material. Surface areas deduced from the data are shown in Table 1.

Table 1. $SrSnO_3$ and $SrSnO_3$-MWCNT Surface Areas

material	BET surface area, m^2/g
$SrSnO_3$	120.00
$SrSnO_3$-MWCNT-1 wt %	126.00
$SrSnO_3$-MWCNT-2 wt %	131.00
$SrSnO_3$-MWCNT-3 wt %	138.00
$SrSnO_3$-MWCNT-4 wt %	139.00

$SrSnO_3$, $SrSnO_3$@MWCNT-1 wt %, $SrSnO_3$@MWCNT-2 wt %, $SrSnO_3$@MWCNT-3 wt %, and $SrSnO_3$@MWCNT-4 wt % have BET surface areas of 120, 126, 131, 138, and 139 m^2/g, respectively. $SrSnO_3$ has a surface area of 120 m^2/g as the synthesis procedure produces a strong mesoporous structure. With the incorporation of a higher surface area MWCNT, the resultant $SrSnO_3$@MWCNT nanocomposite has a BET surface area larger than pure $SrSnO_3$.

$SrSnO_3$ absorbs light in the ultraviolet region as can be seen in Figure 5. Upon incorporation of MWCNTs, absorption of all the $SrSnO_3$@MWCNT samples occurs in the visible region, this will result in the enhancement of light-harvesting ability of the material in a photocatalytic reaction. The UV−vis spectra can also be used to deduce the band gap energies of the material under investigation. Table 2 shows a gradual reduction in band gap energy on going from pure $SrSnO_3$ to an increasing MWCNT content, and the band gap values of
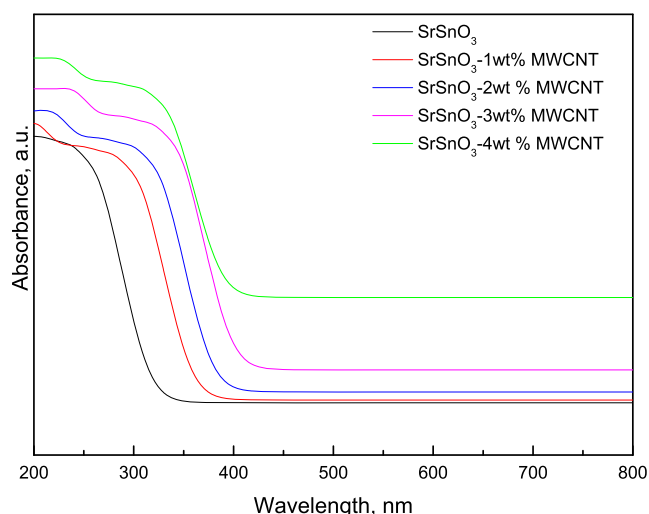

Figure 5. UV−Vis spectra of $SrSnO_3$ and $SrSnO_3$@MWCNT.

Table 2. Band gap Energy Values

sample	band gap energy, eV
$SrSnO_3$	3.68
SrSnO3-MWCNT-1 wt %	3.24
SrSnO3-MWCNT-2 wt %	3.00
SrSnO3-MWCNT-3 wt %	2.86
SrSnO3-MWCNT-4 wt %	2.85

3.68, 3.24, 3.00, 2.86, and 2.85 eV for $SrSnO_3$, $SrSnO_3$@MWCNT-1 wt %, $SrSnO_3$@MWCNT-2 wt %, $SrSnO_3$@MWCNT-3 wt %, and $SrSnO_3$@MWCNT-4 wt %, respectively, clearly show this trend, which favors absorption of visible light thus increasing the photocatalytic performance of the nanocomposite. The PL spectra also confirm absorption in the visible region and a reduction of band gap energies upon addition of the MWCNTs to $SrSnO_3$. As shown in Figure 6, all $SrSnO_3$@MWCNT samples have visible region emission showing that addition of MWCNTs to $SrSnO_3$ shifts the emission peak of $SrSnO_3$ from the ultraviolet to the visible region. Compatible bandgap energies of 3.69, 3.25, 3.01, 2.87,
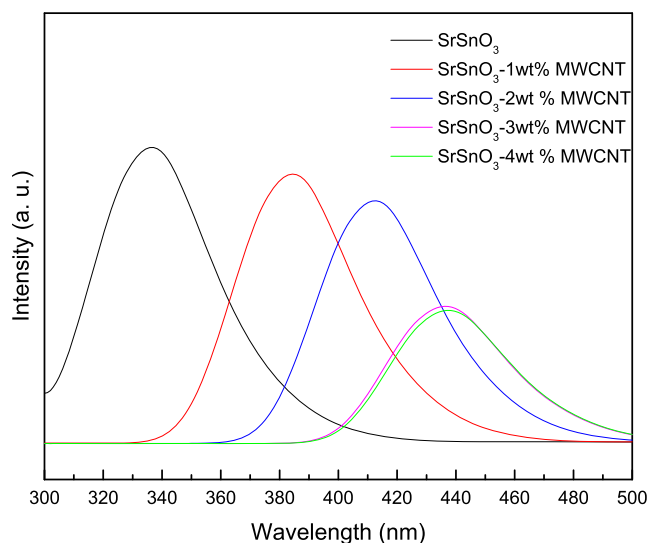

Figure 6. PL spectra of $SrSnO_3$ and $SrSnO_3$@MWCNT.

and 2.86 eV for $SrSnO_3$, $SrSnO_3$@MWCNT-1 wt %, $SrSnO_3$@MWCNT-2 wt %, $SrSnO_3$@MWCNT-3 wt %, and $SrSnO_3$@MWCNT-4 wt % were also deduced from the PL spectra. The reduction of band gap energy is a direct result of adjusting the weight percent of MWCNTs that significantly red-shifted the PL spectra of the nanocomposite photocatalysts. The $SrSnO_3$@MWCNT samples have photocurrent response values greater than pure $SrSnO_3$ (Figure 7), this translates to lower electron–hole recombination rates, which directly manifest in enhanced photocatalytic activity.
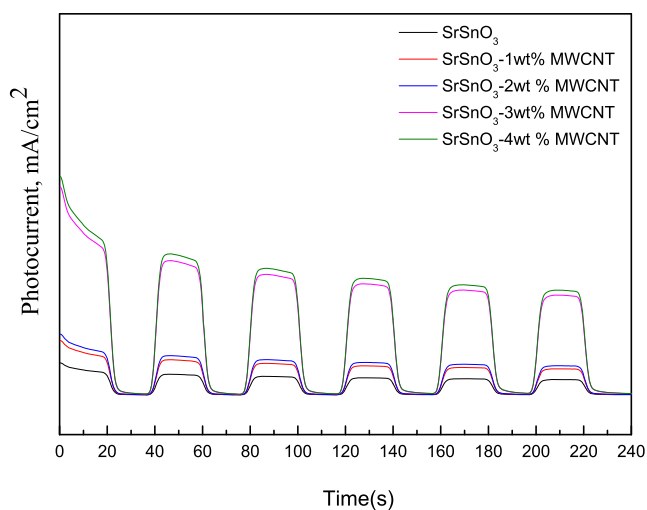

Figure 7. Photocurrent response of $SrSnO_3$ and $SrSnO_3$@MWCNT.

3.2. Hydrogen Production Using $SrSnO_3$@MWCNT Photocatalysts.
Using 1.2 g L^{-1} of pure $SrSnO_3$ and $SrSnO_3$@MWCNT photocatalysts, efficiency of the water splitting reaction was studied with 9 h visible light illumination as shown in Figure 8. The hydrogen production efficiency was
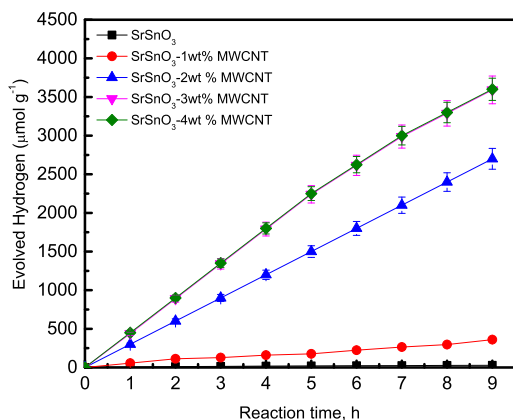

Figure 8. Hydrogen production efficiency employing 1.2 g L^{-1} of $SrSnO_3$ and $SrSnO_3$@MWCNT and 9 h visible light illumination.

very small when $SrSnO_3$ was used, the main reason being its limited light absorption in the UV region. The hydrogen production efficiency for $SrSnO_3$@MWCNT increased over time (Figure 8). The hydrogen production efficiency was enhanced for the MWCNT-supported $SrSnO_3$ to 360 and 2700 μmol g^{-1} for 1.0 and 2.0 wt % MWCNT loadings and reached 3592 μmol g^{-1} for $SrSnO_3$@MWCNT-3 wt % (Figure 8). An important factor that contributed to the enhancement

of the photocatalytic efficiency of $SrSnO_3$ is the incorporation of the MWCNT content, which improves the light absorption efficiency, increases the surface area and hence the active sites available for the reaction, effective charge carrier separation ability, and improves the surface texture. The 3% MWCNT content was proved to be the optimal content that produces highest desired improvements.

The effect of varying the quantity of $SrSnO_3$@MWCNT-3 wt % added to the photocatalytic reaction was studied, and the trends are shown in Figure 9. A range of concentrations
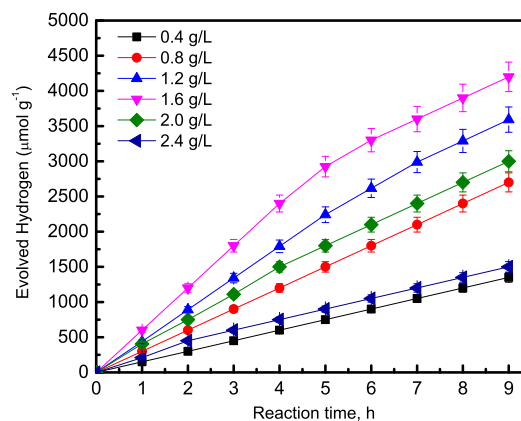

Figure 9. Effect of $SrSnO_3$@MWCNT-3 wt % photocatalyst quantity on the hydrogen production efficiency.

between 0.4 and 2.4 g L^{-1} were utilized. A photocatalyst load range starting from 0.4 to 1.6 g L^{-1} results in an enhancement of the yield from 1350 to 4200 μmol g^{-1}. However, a further increase of doses to 2.0 and 2.4 g L^{-1} results in a drop of hydrogen production efficiency to 3000 and 1500 μmol g^{-1}, respectively. Obstruction of light penetration to reach active species may be a reason for a high number of photocatalyst particles at high concentrations. The photocatalytic hydrogen evolution utilizing the adjusted photocatalyst dose is superior than the current published results of similar nanocomposites as shown in Table S1.

Consistent photocatalytic efficiency was achieved even when the $SrSnO_3$@MWCNT-3 wt % heterojunction was used in five consecutive experiments (Figure 10). After five-time regeneration, the structural properties show no significant change. This was asserted by XRD and XPS investigations (Figure S2, Supporting Information). Furthermore, no loss of the Sr or Sn content was detected in the residual reaction solutions proving that the photocatalyst material remained intact.

3.3. Proposed Photocatalytic Action.
A schematic representation of a viable mechanism of the hydrogen production reaction is presented in Figure 11. In the first step, photons with energy greater than the $SrSnO_3$ band gap energy produce electrons at the conduction band and positive holes at the valence band

$$SrSnO_3 + h\nu (\geq 2.86 \text{ eV}) \rightarrow e_{CB}^- + h_{VB}^+ \qquad (1)$$
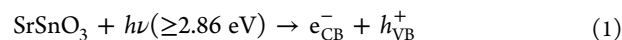
Upon production, the electrons get scavenged by the MWCNT, which plays a sink-like role, resulting in the much-desired charge-carrier separation

$$e_{CB}^-(SrSnO_3) \rightarrow e_{CB}^-(MWCNT) \qquad (2)$$

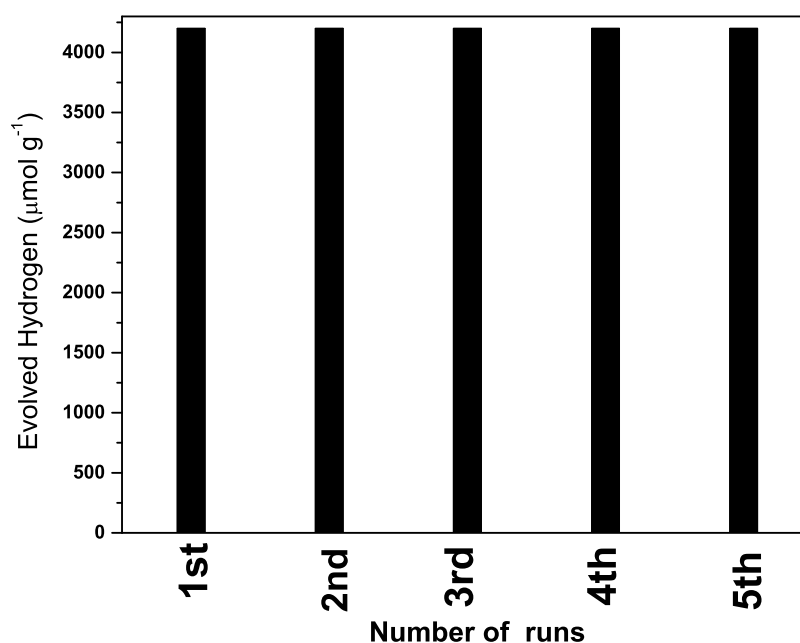In the following step, radicals are readily produced resulting in the completion of hydrogen production

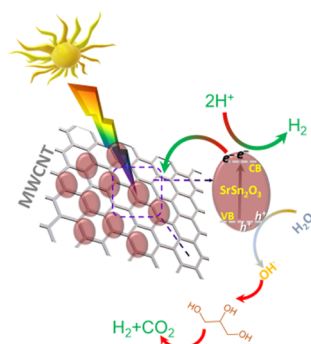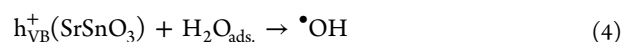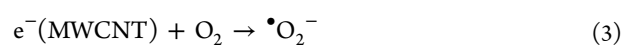**Figure 10.** Effect of SrSnO$_3$@MWCNT-3 wt % reuse on its efficiency.

Figure 11. A schematic of the proposed hydrogen production mechanism employing SrSnO$_3$@MWCNT.

$$e^-(\text{MWCNT}) + O_2 \rightarrow {}^{\bullet}O_2{}^- \qquad (3)$$

$$h_{VB}^+(\text{SrSnO}_3) + H_2O_{\text{ads.}} \rightarrow {}^{\bullet}OH \qquad (4)$$

4. CONCLUSIONS

A facile one-step sol–gel route for the synthesis of SrSnO$_3$ nanoparticles is introduced in this paper. The synthesized SrSnO$_3$ is then utilized to produce a SrSnO$_3$@MWCNT photocatalyst. The incorporation of MWCNTs has a great effect on several properties of SrSnO$_3$ nanoparticles that include structural, optical, and optoelectronic properties. In the synthesized heterojunction, MWCNTs were consistently dispersed and led to a higher surface area of the material. The band gap energy of SrSnO$_3$@MWCNT was close to the desired value of ~2.86 eV. Light absorption ability was significantly improved with exceptional charge-carrier separation ability. Using a 1.6 g L^{-1} photocatalyst dose and a 9 h reaction time, a hydrogen yield of 4200 μmol g^{-1} was achieved. SrSnO$_3$@MWCNT shows remarkable stability upon reuse and its structural integrity does not get compromised with regeneration.

ASSOCIATED CONTENT

Supporting Information

The Supporting Information is available free of charge at https://pubs.acs.org/doi/10.1021/acsomega.1c04143.

Comparison of the recently published results for photocatalytic evolution of H$_2$ with the results of this present study; XRD pattern; and high-resolution XPS spectra (PDF)

AUTHOR INFORMATION

Corresponding Author

Reda M. Mohamed − *Department of Chemistry, Faculty of Science, King Abdulaziz University, Jeddah 21589, Kingdom of Saudi Arabia; Advanced Materials Department, Central Metallurgical R&D Institute, CMRDI, Helwan 11421, Egypt;* ◯ orcid.org/0000-0002-6182-6880; Email: redama123@yahoo.com

Author

Mohammad W. Kadi − *Department of Chemistry, Faculty of Science, King Abdulaziz University, Jeddah 21589, Kingdom of Saudi Arabia*

Complete contact information is available at:
https://pubs.acs.org/10.1021/acsomega.1c04143

Notes

The authors declare no competing financial interest.

■ REFERENCES

(1) Christoforidis, K. C.; Fornasiero, P. Photocatalytic hydrogen production: a rift into the future energy supply. *ChemCatChem* 2017, 9, 1523−1544.

(2) Jafari, T.; Moharreri, E.; Amin, A.; Miao, R.; Song, W.; Suib, S. Photocatalytic Water Splitting-The Untamed Dream: A Review of Recent Advances. *Molecules* 2016, 21, 900.

(3) Li, Q.; Guo, B.; Yu, J.; Ran, J.; Zhang, B.; Yan, H.; Gong, J. R. Highly efficient visible-light-driven photocatalytic hydrogen production of CdS-cluster-decorated graphene nanosheets. *J. Am. Chem. Soc.* 2011, 133, 10878−10884.

(4) Zhang, F.; Zhao, P.; Niu, M.; Maddy, J. The survey of key technologies in hydrogen energy storage. *Int. J. Hydrogen Energy* 2016, 41, 14535−14552.

(5) Zini, G.; Tartarini, P. *Solar Hydrogen Energy Systems: Science and Technology for the Hydrogen Economy*; Springer Science & Business Media, 2012.

(6) Gholipour, M. R.; Nguyen, C. C.; Béland, F.; Do, T.-O. Hollow microspheres consisting of uniform ZnxCd1-xS nanoparticles with noble-metal-free co-catalysts for hydrogen evolution with high quantum efficiency under visible light. *J. Photochem. Photobiol., A* 2018, 358, 1−9.

(7) Ma, Y.; Wang, X.; Jia, Y.; Chen, X.; Han, H.; Li, C. Titanium dioxide-based nanomaterials for photocatalytic fuel generations. *Chem. Rev.* 2014, 114, 9987−10043.

(8) Fujishima, A.; Honda, K. Electrochemical photolysis of water at a semiconductor electrode. *Nature* 1972, 238, 37−38.

(9) Fujishima, A.; Honda, K. Electrochemical photolysis of water at a semiconductor electrode. *nature* 1972, 238, 37−38.

(10) Gupta, S. M.; Tripathi, M. A review of TiO2 nanoparticles. *Chin. Sci. Bull.* 2011, 56, 1639−1657.

(11) Reza Gholipour, M.; Dinh, C.-T.; Béland, F.; Do, T.-O. Nanocomposite heterojunctions as sunlight-driven photocatalysts for hydrogen production from water splitting. *Nanoscale* 2015, 7, 8187−8208.

(12) Lewis, N. S.; Crabtree, G.; Nozik, A. J.; Wasielewski, M. R.; Alivisatos, P.; Kung, H.; Tsao, J.; Chandler, E.; Walukiewicz, W.; Spitler, M.; Ellingson, R. *Basic Research Needs for Solar Energy Utilization. Report of the Basic Energy Sciences Workshop on Solar Energy Utilization, April 18−21, 2005*; DOESC (USDOE Office of Science (SC)), 2005; pp 18−21.

(13) Panwar, N. L.; Kaushik, S. C.; Kothari, S. Role of renewable energy sources in environmental protection: A review. *Renew. Sustain. Energy Rev.* 2011, 15, 1513−1524.

(14) Šojić, D.; Despotović, V.; Abramović, B.; Todorova, N.; Giannakopoulou, T.; Trapalis, C. Photocatalytic degradation of mecoprop and clopyralid in aqueous suspensions of nanostructured N-doped TiO2. *Molecules* 2010, 15, 2994−3009.

(15) Liu, S.; Yu, J.; Cheng, B.; Jaroniec, M. Fluorinated semiconductor photocatalysts: tunable synthesis and unique properties. *Adv. Colloid Interface Sci.* 2012, 173, 35−53.

(16) Liu, S.; Yu, J.; Jaroniec, M. Anatase TiO2 with Dominant High-Energy {001} Facets: Synthesis, Properties, and Applications. *Chem. Mater.* 2011, 23, 4085−4093.

(17) Shin, S. S.; Yeom, E. J.; Yang, W. S.; Hur, S.; Kim, M. G.; Im, J.; Seo, J.; Noh, J. H.; Seok, S. I. Colloidally prepared La-doped BaSnO3 electrodes for efficient, photostable perovskite solar cells. *Science* 2017, 356, 167−171.

(18) Kudo, A.; Miseki, Y. Heterogeneous photocatalyst materials for water splitting. *Chem. Soc. Rev.* 2009, 38, 253−278.

(19) Ansari, F.; Nazari, P.; Payandeh, M.; Asl, F. M.; Abdollahi-Nejand, B.; Ahmadi, V.; Taghiloo, J.; Salavati-Niasari, M. Novel nanostructured electron transport compact layer for efficient and large-area perovskite solar cells using acidic treatment of titanium layer. *Nanotechnology* 2018, 29, 075404.

(20) Masjedi-Arani, M.; Salavati-Niasari, M. Ultrasonic assisted synthesis of a nano-sized Co2SnO4/graphene: A potential material for electrochemical hydrogen storage application. *Int. J. Hydrogen Energy* 2018, 43, 4381−4392.

(21) Seong, W. M.; Park, K.-Y.; Lee, M. H.; Moon, S.; Oh, K.; Park, H.; Lee, S.; Kang, K. Abnormal self-discharge in lithium-ion batteries. *Energy Environ. Sci.* 2018, 11, 970−978.

(22) Zhang, W. F.; Tang, J.; Ye, J. Photoluminescence and photocatalytic properties of SrSnO3 perovskite. *Chem. Phys. Lett.* 2006, 418, 174−178.

(23) Meng, L.; Chen, Z.; Ma, Z.; He, S.; Hou, Y.; Li, H.-H.; Yuan, R.; Huang, X.-H.; Wang, X.; Wang, X.; Long, J. Gold plasmon-induced photocatalytic dehydrogenative coupling of methane to ethane on polar oxide surfaces. *Energy Environ. Sci.* 2018, 11, 294−298.

(24) Chen, D.; Ye, J. SrSnO3 Nanostructures: Synthesis, Characterization, and Photocatalytic Properties. *Chem. Mater.* 2007, 19, 4585−4591.

(25) Ghanbari, M.; Ansari, F.; Salavati-Niasari, M. Simple synthesis-controlled fabrication of thallium cadmium iodide nanostructures via a novel route and photocatalytic investigation in degradation of toxic dyes. *Inorg. Chim. Acta* 2017, 455, 88−97.

(26) Morassaei, M. S.; Zinatloo-Ajabshir, S.; Salavati-Niasari, M. New facile synthesis, structural and photocatalytic studies of NdOCl-Nd2Sn2O7-SnO2 nanocomposites. *J. Mol. Liq.* 2016, 220, 902−909.

(27) Zinatloo-Ajabshir, S.; Morassaei, M. S.; Salavati-Niasari, M. Facile fabrication of Dy 2 Sn 2 O 7 -SnO 2 nanocomposites as an effective photocatalyst for degradation and removal of organic contaminants. *J. Colloid Interface Sci.* 2017, 497, 298−308.

(28) Masjedi-Arani, M.; Salavati-Niasari, M. Simple size-controlled fabrication of Zn2SnO4 nanostructures and study of their behavior in dye sensitized solar cells. *Int. J. Hydrogen Energy* 2017, 42, 858−866.

(29) Hadjarab, B.; Bouguelia, A.; Trari, M. Synthesis, physical and photo electrochemical characterization of La-doped SrSnO3. *J. Phys. Chem. Solid* 2007, 68, 1491−1499.

(30) Gu, Q.; Long, J.; Zhuang, H.; Zhang, C.; Zhou, Y.; Wang, X. Ternary Pt/SnOx/TiO2 photocatalysts for hydrogen production: consequence of Pt sites for synergy of dual co-catalysts. *Phys. Chem. Chem. Phys.* 2014, 16, 12521−12534.

(31) Woodward, P. M. Octahedral tilting in perovskites. II. Structure stabilizing forces. *Acta Crystallogr., Sect. B: Struct. Sci.* 1997, 53, 44−46.

(32) Kudo, A.; Kato, H.; Nakagawa, S. Water splitting into H2 and O2 on new Sr2M2O7 (M= Nb and Ta) photocatalysts with layered perovskite structures: factors affecting the photocatalytic activity. *J. Phys. Chem. B* 2000, 104, 571−575.

(33) Lee, C. W.; Kim, D. W.; Cho, I. S.; Park, S.; Shin, S. S.; Seo, S. W.; Hong, K. S. Simple synthesis and characterization of SrSnO3 nanoparticles with enhanced photocatalytic activity. *Int. J. Hydrogen Energy* 2012, 37, 10557−10563.

(34) Alammar, T.; Hamm, I.; Grasmik, V.; Wark, M.; Mudring, A.-V. Microwave-Assisted Synthesis of Perovskite SrSnO3 Nanocrystals in Ionic Liquids for Photocatalytic Applications. *Inorg. Chem* 2017, 56, 6920−6932.

(35) Wu, T.; Lin, T.; Zhao, J.; Hidaka, H.; Serpone, N. TiO2-Assisted Photodegradation of Dyes. 9. Photooxidation of a Squarylium Cyanine Dye in Aqueous Dispersions under Visible Light Irradiation. *Environ. Sci. Technol.* 1999, 33, 1379−1387.

(36) Shimizu, Y.; Shimabukuro, M.; Arai, H.; Seiyama, T. Humidity-Sensitive Characteristics of La3+-Doped and Undoped SrSnO3. *J. Electrochem. Soc.* 1989, 136, 1206.

(37) Hu, X.; Tang, Y.; Xiao, T.; Jiang, J.; Jia, Z.; Li, D.; Li, B.; Luo, L. Rapid Synthesis of Single-Crystalline SrSn(OH)6 Nanowires and the Performance of SrSnO3 Nanorods Used as Anode Materials for Li-Ion Battery. *J. Phys. Chem. C* 2010, 114, 947−952.

(38) Doroftei, C.; Popa, P. D.; Iacomi, F. Preparation and study of structural properties of zinc-doped barium stannate. *J. Optoelectron. Adv. Mater.* 2012, 14, 413−417.

(39) Udawatte, C. P.; Kakihana, M.; Yoshimura, M. Low temperature synthesis of pure SrSnO3 and the (BaxSr1−x) SnO3 solid solution by the polymerized complex method. *Solid State Ionics* 2000, 128, 217−226.

(40) Zhao, X.; Yang, H.; Cui, Z.; Yi, Z.; Yu, H. Synergistically enhanced photocatalytic performance of Bi4Ti3O12 nanosheets by Au and Ag nanoparticles. *J. Mater. Sci.: Mater. Electron.* **2019**, *30*, 13785−13796.

(41) Yi, Z.; Li, X.; Wu, H.; Chen, X.; Yang, H.; Tang, Y.; Yi, Y.; Wang, J.; Wu, P. Fabrication of ZnO@Ag3PO4 Core-Shell Nano-composite Arrays as Photoanodes and Their Photoelectric Properties. *Nanomaterials* **2019**, *9*, 1254.

(42) Xia, Y.; He, Z.; Hu, K.; Tang, B.; Su, J.; Liu, Y.; Li, X. Fabrication of n-SrTiO3/p-Cu2O heterojunction composites with enhanced photocatalytic performance. *J. Alloys Compd.* **2018**, *753*, 356−363.

(43) Wang, S.; Yang, H.; Wang, X.; Feng, W. Surface Disorder Engineering of Flake-Like Bi2WO6 Crystals for Enhanced Photo-catalytic Activity. *J. Electron. Mater.* **2019**, *48*, 2067−2076.

(44) Ahmadi, M.; Ramezani Motlagh, H.; Jaafarzadeh, N.; Mostoufi, A.; Saeedi, R.; Barzegar, G.; Jorfi, S. Enhanced photocatalytic degradation of tetracycline and real pharmaceutical wastewater using MWCNT/TiO2 nano-composite. *J. Environ. Manag.* **2017**, *186*, 55−63.

(45) Wang, S.; Gao, H.; Wei, Y.; Li, Y.; Yang, X.; Fang, L.; Lei, L. Insight into the optical, color, photoluminescence properties, and photocatalytic activity of the N-O and C-O functional groups decorating spinel type magnesium aluminate. *CrystEngComm* **2019**, *21*, 263−277.

(46) Cai, C.; Han, S.; Liu, W.; Sun, K.; Qiao, L.; Li, S.; Zu, X. Tuning catalytic performance by controlling reconstruction process in operando condition. *Appl. Catal., B* **2020**, *260*, 118103.

(47) Gao, H.; Wang, F.; Wang, S.; Wang, X.; Yi, Z.; Yang, H. Photocatalytic activity tuning in a novel Ag2S/CQDs/CuBi2O4 composite: Synthesis and photocatalytic mechanism. *Mater. Res. Bull.* **2019**, *115*, 140−149.

(48) Di, L.; Xian, T.; Sun, X.; Li, H.; Zhou, Y.; Ma, J.; Yang, H. Facile Preparation of CNT/Ag2S Nanocomposites with Improved Visible and NIR Light Photocatalytic Degradation Activity and Their Catalytic Mechanism. *Micromachines* **2019**, *10*, 503.

(49) Esmaeili, A.; Entezari, M. H. Sonosynthesis of an Ag/AgBr/Graphene-oxide nanocomposite as a solar photocatalyst for efficient degradation of methyl orange. *J. Colloid Interface Sci.* **2016**, *466*, 227−237.

(50) Karmaoui, M.; Lajaunie, L.; Tobaldi, D. M.; Leonardi, G.; Benbayer, C.; Arenal, R.; Labrincha, J. A.; Neri, G. Modification of anatase using noble-metals (Au, Pt, Ag): Toward a nanoheter-ojunction exhibiting simultaneously photocatalytic activity and plasmonic gas sensing. *Appl. Catal., B* **2017**, *218*, 370−384.

(51) Xian, T.; Di, L.; Sun, X.; Li, H.; Zhou, Y.; Yang, H. Photo-Fenton Degradation of AO7 and Photocatalytic Reduction of Cr(VI) over CQD-Decorated BiFeO3 Nanoparticles Under Visible and NIR Light Irradiation. *Nanoscale Res. Lett.* **2019**, *14*, 397.

(52) Ahmadi, M.; Ramezani Motlagh, H.; Jaafarzadeh, N.; Mostoufi, A.; Saeedi, R.; Barzegar, G.; Jorfi, S. Enhanced photocatalytic degradation of tetracycline and real pharmaceutical wastewater using MWCNT/TiO2 nano-composite. *J. Environ. Manage.* **2017**, *186*, 55−63.

(53) Wang, H.-L.; Li, Y.; Pang, L.; Zhang, W.-Z.; Jiang, W.-F. Preparation and application of thermosensitive poly(NIPAM-co-MAH-β-CD)/(TiO2-MWCNTs) composites for photocatalytic deg-radation of dinitro butyl phenol (DNBP) under visible light irradiation. *Appl. Catal., B* **2013**, *130−131*, 132−142.

(54) Sedghi, R.; Heidari, F. A novel & effective visible light-driven TiO2/magnetic porous graphene oxide nanocomposite for the degradation of dye pollutants. *RSC Adv.* **2016**, *6*, 49459−49468.

(55) Ortega-Liebana, M. C.; Hueso, J. L.; Ferdousi, S.; Arenal, R.; Irusta, S.; Yeung, K. L.; Santamaria, J. Extraordinary sensitizing effect of co-doped carbon nanodots derived from mate herb: Application to enhanced photocatalytic degradation of chlorinated wastewater compounds under visible light. *Appl. Catal., B* **2017**, *218*, 68−79.

(56) Gui, M. M.; Chai, S.-P.; Xu, B.-Q.; Mohamed, A. R. Visible-light-driven MWCNT@TiO2 core-shell nanocomposites and the roles of MWCNTs on the surface chemistry, optical properties and reactivity in CO2 photoreduction. *RSC Adv.* **2014**, *4*, 24007−24013.

(57) Bouazza, N.; Ouzzine, M.; Lillo-Ródenas, M. A.; Eder, D.; Linares-Solano, A. TiO$_2$ nanotubes and CNT−TiO$_2$ hybrid materials for the photocatalytic oxidation of propene at low concentration. *Appl. Catal., B* **2009**, *92*, 377−383.

(58) Yu, J.; Ma, T.; Liu, S. Enhanced photocatalytic activity of mesoporous TiO2aggregates by embedding carbon nanotubes as electron-transfer channel. *Phys. Chem. Chem. Phys.* **2011**, *13*, 3491−3501.